JOURNAL OF SPACECRAFT AND ROCKETS
Vol. 39, No. 4, July–August 2002

Coupled Aeroheating/Ablation Analysis for Missile Configurations

A. L. Murray*
ITT Aerotherm, Huntsville, Alabama 35806
and
G. W. Russell†
U.S. Army Aviation and Missile Command, Huntsville, Alabama 35898

A method for high-fidelity surface temperature and thermal transient calculations for missile configurations is described. The key technical requirements for these predictions are accurate heat transfer coefficient distributions as functions of time and a coupled, transient thermal solution. These requirements have been met by integrating the capabilities of two computer codes. The Maneuvering Aerotherm Shape Change Code is used to determine the convective boundary conditions based on a prescribed trajectory. At each time step, these boundary conditions are applied to the surface nodes. The Charring Material Thermal Response and Ablation Program is used to determine the conduction of heat into the body, the charring of the materials, and ablation from the surface during the time step. This explicit coupling is continued throughout the entire flight. The methodology is verified with comparisons to the arc heater and flight-test data. A final demonstration of the code's capability is shown with a lethality sled test on an airframe prototype subjected to multiple environmental mediums (air/helium).

Nomenclature

A = reference area, m^2
B' = nondimensional mass loss rate, $\dot{m}/\rho_e u_e C_M$
$C_f/2$ = friction factor, $\tau_w/\rho_e u_e^2$
C_h = Stanton number
C_M = mass transfer coefficient
c_p = specific heat at constant pressure, J/kg · K
F = entrainment shape factor, $(\delta - \delta_e^*)/\Theta$; radiation view factor
H = shape factor, δ^*/Θ
h = enthalpy, J/kg
h_g = enthalpy of pyrolysis gas, J/kg
h_r = recovery enthalpy, J/kg
h_s = enthalpy of surface material, J/kg
h_t = total enthalpy, identical to $h + u^2/2$, J/kg
h_w = wall enthalpy, J/kg
$I_{x,y,z}$ = influence coefficient
k = thermal conductivity, W/m · K
$\dot{m}$ = mass flux, kg/s
$\hat{n}$ = surface normal unit vector
Pr = Prandtl number
p = pressure, N/m^2
$\dot{q}_{\text{cond}}$ = conduction heat flux into material, W/m^2
$\dot{q}_{\text{rad}}$ = radiation heat flux, W/m^2
$\dot{q}_w$ = wall heat flux, W/m^2
R = recovery factor; gas constant, J/kg · K
Re = Reynolds number
r = radial coordinate, m
s = stream length measured from the stagnation point, m
$\dot{s}$ = recession rate in the surface normal direction, m/s
T = temperature, K
u = boundary-layer flow velocity tangent to surface, m/s
$\boldsymbol{V}_\infty$ = freestream velocity vector, m/s
v = boundary-layer flow velocity normal to surface, m/s
$\boldsymbol{v}$ = tangential velocity vector, m/s
x = coordinate normal to ablating surface with origin fixed in space, m
$\bar{y}$ = shock radial location through which boundary-layer edge streamline passes, m
Z_i = diffusion driving potential
z = coordinate normal to ablating surface with origin fixed to the receding surface, m
δ = boundary-layer thickness, m
δ^* = boundary-layer displacement thickness, m

$$\int_0^\delta 1 - \left(\frac{\rho u}{\rho_e u_e}\right) \mathrm{d}y$$

ε = surface emissivity
Θ = boundary-layer momentum thickness, m
θ = time, s
μ = viscosity, kg/m · s
ρ = density, kg/m^3
Φ = energy thickness, m

$$\int_0^\delta \frac{\rho u}{\rho_e u_e}\left(\frac{h_{t,i} - h_t}{h_{t,e} - h_w}\right) \mathrm{d}y$$

Subscripts

c = char property
e = boundary-layer edge
g = pyrolysis gas property
ℓ = laminar flow
t = turbulent flow
w = wall

Introduction

THE purpose of this paper is to describe a process for predicting the aeroheating and thermal response of typical missile configurations in high-speed flows. These predictions are the required inputs to determine the survivability of a conceptual design and to provide a needed evaluation of a design without having to build multiple prototypes for testing and evaluation. The flight regime of most interest is that of supersonic–hypersonic continuum flow in which the heat flux is sufficient to cause ablation at some locations on the surface.

Received 14 September 2000; revision received 1 November 2001; accepted for publication 9 November 2001.

*Senior Principal Engineer, Aerothermal Sciences. Senior Member AIAA.
†Engineer, Propulsion and Structures Directorate. Member AIAA.

Boundary conditions generated during a specified flight were determined using the Maneuvering Aerotherm Shape Change Code (MASCC[1]). At each time step, these boundary conditions were applied to a Charring Material Thermal Response and Ablation Program (CMA[2]) finite difference model to obtain the transient thermal response at each of the surface nodes. Thus, the changes in the surface temperature, ablation and pyrolysis mass fluxes, and the shape of the missile are incorporated into the next flowfield solution. This integration is continued throughout the entire flight. The following section gives a brief description of the coupled code.

Flowfield Analysis

MASCC includes a completely general three-dimensional flowfield solver that uses semiempirical procedures to determine the flowfield on missile configurations. The code offers significant efficiency advantages for design purposes over computational fluid dynamics (CFD) codes that solve the full Navier–Stokes equations. The hundreds of flowfield and boundary-layer solutions that are required to model a complete trajectory require less than 1 h with MASCC. CFD techniques, on the other hand, would require very fine grids to resolve boundary layers, and this would result in extremely long run times to model the many different flight conditions that must be considered. Ideally, CFD techniques can be used in concert with MASCC to refine specific areas of complex flowfield phenomena and shock interactions when necessary.

MASCC can be used to calculate the surface heat flux based on the velocity, altitude, and angle of attack throughout the flight of interest. The basic inputs needed are the body geometry, angle of attack, and the freestream conditions. The geometry is described in MASCC with a system of Coons and Herzog's bicubic patches.[3] These patches allow general geometries and facilitate the calculation of the surface coordinates and gradients at points intermediate to the nodal system. In MASCC, the axisymmetric analogy is used for the prediction of the flowfield. With this approximation, the axisymmetric equations for the inviscid and viscous flow are integrated along various streamlines. An effective radius, or metric coefficient, replaces the radius r in the axisymmetric equations.

Inviscid Streamline Tracing

The flowfield solution is performed along each of the calculated inviscid streamlines. The method used in MASCC to calculate these streamlines is known as the Newtonian approximation, or the method of steepest descent. The Newtonian flow model assumes that a stream of particles impinging on a surface retains its tangential component of momentum. Therefore, an instantaneous velocity direction at each point on the body is defined by

$$\boldsymbol{v} = \hat{n} \times (\boldsymbol{V}_\infty \times \hat{n})$$

By the conversion of $\boldsymbol{v}$ to a unit tangent vector, the derivatives of the surface parameters with respect to the streamline arc length may be determined in the following manner. If $\boldsymbol{r}$ is the position vector of some point on the body, the parametric representation of the body geometry provides $\boldsymbol{r}$ as a function of the surface parameter w and u. The unit tangent vector at the point may then be written

$$\hat{t} = \frac{\mathrm{d}\boldsymbol{r}}{\mathrm{d}s} = \frac{\partial \boldsymbol{r}}{\partial w}\frac{\mathrm{d}w}{\mathrm{d}s} + \frac{\partial \boldsymbol{r}}{\partial u}\frac{\mathrm{d}u}{\mathrm{d}s} \tag{1}$$

Any two of the three Eqs. (1) may be solved for $\mathrm{d}w/\mathrm{d}s$ and $\mathrm{d}u/\mathrm{d}s$, the slopes in each of the two surface coordinate directions. This algorithm can be started at any point on the body and integrated either upstream or downstream.

One of the most difficult problems in coupling a shape change procedure with a three-dimensional flowfield analysis is an accurate prediction of the environment at each shape change point. With a streamline tracing procedure, such as the one used in MASCC, this problem is even more complicated because the location of the streamlines is difficult to control as the nosetip ablates. The MASCC procedure begins at the back of the vehicle and traces a streamline forward to the stagnation point. This assures a reasonable distribution at the end of the vehicle and eliminates the effects of the ablated nosetip on the streamlines. To provide adequate coverage at the nosetip, a streamline addition procedure is used that establishes additional streamlines on the leeward side of the vehicle.

Surface Pressure

The MASCC code has three options for computing surface pressure distributions on the windward streamlines: 1) the Dahm–Love pressure correlations used in ASCC (see Ref. 4), 2) a Newtonian pressure model with modifications for Mach number effects,[5] or 3) a modified Newtonian pressure model for sharp-nosed vehicles.[6] Pressures on the leeward or shadow regions are calculated using 1) the Newtonian approximation ($C_p = 0$), 2) hypersonic small disturbance theory,[7] or 3) a pressure correlation for separated flows.[7] In general, the Dahm–Love correlations are used for blunt, short, sphere–cone geometries. The modified Newtonian model is used for ogives and other sharp-nosed configurations.

Shock Shape

A thin-shock layer integral technique is used in MASCC to compute the shock shape. The global continuity and axial momentum equations are cast in integral form. The global continuity equation is given by

$$\rho_\infty u_\infty \pi R^2 = 2\pi \int_0^{\delta_s} \rho u r \,\mathrm{d}y$$

and the global axial momentum by

$$\left(p_\infty + \rho_\infty u_\infty^2\right)\pi R^2 = \int_0^{\delta_s} \rho u (u\cos\theta + v\sin\theta) 2\pi r \,\mathrm{d}y$$

$$+ \int_0^{s} (p_w \sin\theta) 2\pi r_w \,\mathrm{d}s + \int_0^{\delta_t} (p\cos\theta) 2\pi r \,\mathrm{d}y$$

The integrands are assumed to vary linearly between the body surface and shock. The flow properties behind the shock are related to freestream conditions via oblique shock relations and the equation of state. With the known pressure distribution along the wall, together with the assumed integrand functional form and behind-the-shock properties, the continuity and axial momentum equations are solved for shock standoff distance and shock angle. The standoff distance and angle are related by geometry, which serves as a boundary condition, rendering an elliptic system of equations that must be iterated for the standoff distance along the body. Decoupling the geometry constraint from the system of equations eliminates the iteration. This approach results in an initial value problem. The control volume for the thin shock layer solution is shown in Fig. 1.

Boundary-Layer Technique

The boundary-layer scheme employed in MASCC is known as the momentum/energy integral technique (MEIT). MEIT has also been used in the ABRES Shape Change Code (ASCC[4]) and three-dimensional momentum/energy integral technique (3DMEIT) codes and is essentially the same in all of these procedures. The current modifications in MASCC incorporate the latest developments in MEIT, and the procedure should be the same as that used in ASCC86, except for the metric coefficient and differences in the body slopes due to the different geometry specification. In MEIT, the baseline relationships are those for C_f and C_h as functions of Re_θ and Re_ϕ

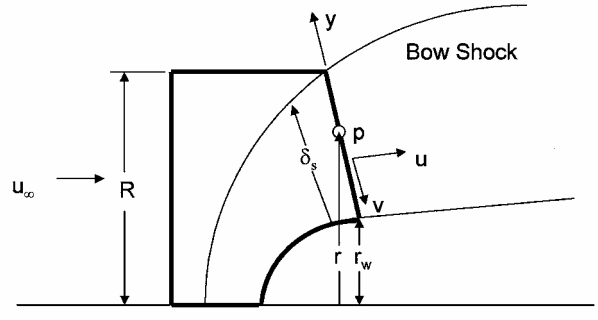

Fig. 1 Control volume for the shock shape solution.

on an incompressible flat plate. The effects of other phenomena are included as multiplicative factors, called influence coefficients, which are applied to the baseline expressions. A theoretical justification for this approach is the work of Kutateladze and Leont'ev[8] and Kutateladze,[9] who show that the asymptotic behavior of the shear and heat transfer for compressible boundary-layer flow over a flat plate in the limit of infinite Reynolds number differ from the corresponding incompressible case by a factor they call Ψ, which is exactly the influence coefficient used in MEIT.

The following three basic equations are solved simultaneously in the MEIT procedure:
The integral momentum equation,

$$\frac{1}{r\rho_e u_e^2}\frac{\mathrm{d}}{\mathrm{d}s}\left(r\rho_e u_e^2\Theta\right) = \frac{C_f}{2} + \frac{(\rho v)_w u_{i,w}}{\rho_e u_e^2} + \frac{H\Theta}{\rho_e u_e^2}\frac{\mathrm{d}p}{\mathrm{d}s} \tag{2}$$

the integral energy equation,

$$\frac{1}{r\rho_e u_e(h_{t,e}-h_w)}\frac{\mathrm{d}}{\mathrm{d}s}[r\rho_e u_e(h_{t,e}-h_w)\Phi]$$

$$= C_h\frac{h_r - h_w}{h_{t,e}-h_w} + \frac{(\rho v)_w(h_{t,i,w}-h_w)}{\rho_e u_e(h_{t,e}-h_w)} \tag{3}$$

and the entrainment relation,

$$\rho_\infty u_\infty \bar{y}^2 = 2rF\mu_e Re_\theta - 2\int_0^\infty r(\rho v)_w\,\mathrm{d}s \tag{4}$$

The momentum equation solution dictates the skin friction and momentum thickness on which the following phenomena are based: 1) transition onset and location, 2) transitional intermittency, 3) surface roughness effects, 4) turbulent boundary-layer shape factors, and 5) entrainment rate. The energy equation solution dictates the convective heat transfer subject to these five parameters.

The entrainment relation, Eq. (4), provides a means of determining the boundary-layer properties that are essential boundary conditions for the solution of Eqs. (2) and (3). The boundary-layeredge thermodynamic state is determined by lookup on pressure and entropy in a real-gas Mollier table. Pressure is known from the inviscid flow solution, and entropy is calculated from consideration of the bow shock shape and boundary-layer mass entrainment. Figure 2 illustrates the method and basis for the mass balance that leads to Eq. (4).

Basic Boundary-Layer Laws

The friction factor and Stanton number are represented by $C_{x,y,0}$, where the subscript 0 denotes the basic laws, with $x = f$ for friction factor and $x = h$ for Stanton number. The state of the boundary layer is shown by the subscript y. The subscript ℓ is used for laminar flow and t for turbulent flow.

Wall Shear and Heat Flux

The basic laws for the friction and Stanton number are for laminar flow,

$$\frac{C_{f,\ell,0}}{2} = \frac{0.220}{Re_\Theta}, \qquad C_{h,\ell,0} = \frac{0.220}{Pr^{\frac{4}{3}}Re_\Phi}$$

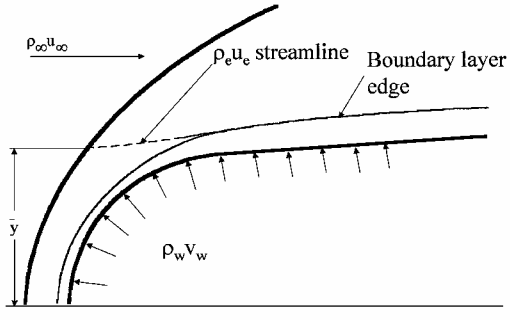

Fig. 2 Sketch of the boundary-layer mass entrainment method.

and turbulent flow,

$$\frac{C_{f,t,0}}{2} = \frac{0.245}{Re_\Theta} + \frac{0.010742Re_\Theta}{100+Re_\Theta}(\log_{10} Re_\Theta)^{-1.5262}$$

$$C_{h,t,0} = \frac{0.22}{Pr^{\frac{4}{3}}Re_\Phi} + \frac{aRe_\Phi}{(100+Re_\Phi)}(\log_{10} Re_\Phi)^{-b}$$

For $Pr \geq 0.6$,

$$a = \frac{0.0993e^{(0.0648Pr)}}{1.0+9.6Pr}, \qquad b = \frac{1.954e^{(0.273Pr)}}{1.0+0.71Pr}$$

and for $Pr < 0.6$,

$$a = \frac{0.1256e^{(0.2435Pr)}}{1.0+14.2Pr}, \qquad b = \frac{2.217e^{(0.6313Pr)}}{1.0+1.677Pr}$$

Boundary-Layer Shape and Recovery Factors

Currently, the shape factors employed in MEIT are based on simplistic laws: 1) zero pressure gradient von Kármán–Polhausen boundary-layer profiles for laminar conditions; 2) profiles of $(1/n)$ power for the turbulent boundary layer, where n is a function of Re; and 3) velocity squared total enthalpy distribution through the boundary layers.

The boundary-layer recovery factor R is needed to compute recovery enthalpies for heat transfer and boundary-layer reference property evaluations. It is defined as

$$R \equiv (h_r - h_e)/(h_{t,e} - h_e)$$

The expressions used to represent the laminar shape and recovery factors are

$$H_\ell = 3.029(\rho_e/\rho_w) - 0.614$$

$$F_\ell = 1.521 + 4.388(\rho_e/\rho_w + 0.0378)^{\frac{1}{2}}, \qquad R_\ell = Pr^{\frac{1}{2}}$$

Additional curve fits for the shape factors H and F in turbulent flow were developed from parametric two-layer boundary-layer profile calculations that used Couette flow with mixing length theory for the inner layer and compressible simple wake theory in the outer layer. The recovery factor for turbulent flow is $R_t = Pr^{1/3}$.

Transitional and Nonideal Effects

For natural transition, the dependence of the parameters $C_f/2$, C_h, H, F, and R (the recovery factor) on the boundary-layer state is established via the transitional intermittency factor. This factor is zero in laminar flow, unity in turbulent flow, and between 0 and 1 for transitional flow. The transitional intermittency that is employed in MASCC is based on the work of Persh, according to the interpretation of Dahm (see Ref. 4).

Nonideal effects are modeled through the use of influence coefficients. These coefficients are factors that are derived by comparing the convective transfer with the ideal flat-plate result for the same boundary-layer state. These factors are generally derived by only one nonideal mechanism at a time. The MEIT procedure assumes that C_h and $C_f/2$ can be written as

$$C_{x,y} = C_{x,y,0}\prod^{z} I_{x,y,z}$$

for $x = h$, f and $y = \ell, t$, where $C_{x,y,0}$ refers to the basic law for incompressible flow along an impervious, isothermal flat plate; x indicates heat or momentum transfer, y indicates laminar or turbulent flow; and z indicates the nonideal effect being considered. Current effects modeled in MASCC include acceleration caused by finite pressure gradients, real gas and Mach number effects, surface roughness, and mass transfer. A complete description of these models is given by Murray.[1]

CMA Transient Thermal Environment

CMA uses an implicit, finite difference procedure for computing the one-dimensional transient transport of thermal energy in a material that can ablate from a front surface and decompose in depth. Figure 3 illustrates the general physical problem treated by CMA. As the material is heated, one or more components of the original composite material pyrolyzes and yields a pyrolysis gas and a porous residue. The pyrolysis gas percolates away from the pyrolysis zone. The residue, for many materials of interest, is a carbonaceous char, possibly reinforced with refractory fibers or cloth.

The in-depth solution procedure is basically a transient heat conduction calculation coupled to a pyrolysis rate calculation and to boundary conditions from the flowfield solution. The coupling with the boundary conditions is provided through a surface energy balance solution.

Decomposition (Pyrolysis or Charring)

Because many decomposing materials appear to behave as three independently pyrolyzing components, the program uses a three-component decomposition model for the surface materials and for any decomposing back-up materials. The resin filler is presumed to consist of two components that decompose separately, whereas the reinforcing material is the third component that can also decompose. The instantaneous density of the composite is given by

$$\rho = \Gamma(\rho_A + \rho_B) + (1 - \Gamma)\rho_C$$

where A and B represent components of the resin, C represents the reinforcing material, and Γ is the volume fraction of the resin. Each of the three components can decompose following the relation

$$\left.\frac{\partial \rho_i}{\partial \theta}\right|_x = -B_i \exp\left(\frac{-E_{a_i}}{RT}\right)\rho_{o_i}\left(\frac{\rho_i - \rho_{r_i}}{\rho_{o_i}}\right)^{\varphi_i}$$

where ρ_{r_i} is the residual density and ρ_{o_i} is the original density of component i. The values B_i, φ_i, and E_{a_i} along with the preceding densities are input parameters for each of the three components of the surface material. A separate set of pyrolysis data may be entered for each decomposing backup material.

In-Depth Thermal Solution

The in-depth energy balance equation is written in a coordinate system tied to the receding surface, as shown in Fig. 4. In this system, the equation becomes

$$\rho c_p \left.\frac{\partial T}{\partial \theta}\right|_z = \frac{1}{A}\frac{\partial}{\partial z}\left(kA\frac{\partial T}{\partial z}\right)_\theta + (h_g - \bar{h})\left.\frac{\partial \rho}{\partial \theta}\right|_x + \dot{s}\rho c_p \left.\frac{\partial T}{\partial z}\right|_\theta + \left.\frac{\dot{m}_g}{A}\frac{\partial h_g}{\partial z}\right|_\theta$$

in which the individual terms represent the rate of sensible energy storage, the net rate of thermal conduction, pyrolysis energy rate, convection rate of sensible energy due to coordinate system movement, and the net rate of energy convected with the pyrolysis gas.

The internal energy equation is computed implicitly for each node, using new temperatures in the heat conduction terms. The energy balance is linked explicitly to the decomposition events, because the pyrolysis gas fluxes are derived from the explicit decomposition calculation. The energy equation is also linked explicitly to the surface boundary condition through the use of the old recession

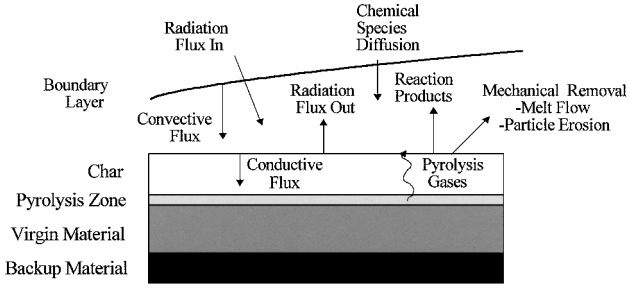

Fig. 3 Schematic of the general surface energy balance.

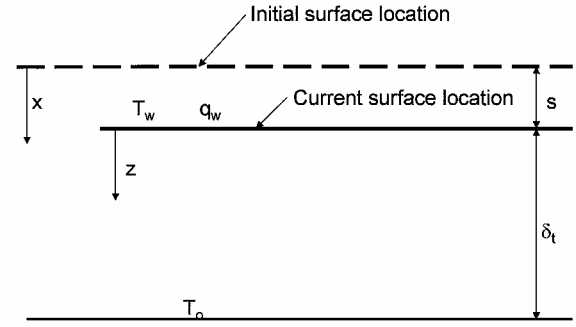

Fig. 4 Coordinate system of the in-depth thermal solution.

rate in all convection terms involving the fluxes of solids. All other links to the surface events are implicit.

The implicit formulation of the in-depth nodal energy equations yields a tridiagonal set of equations that is solved for the unknown temperatures in two passes of direct elimination. The first pass eliminates one unknown from each equation and leaves the equation for the first node with only one unknown, the surface temperature. This unknown temperature is solved using an iterative procedure in the surface energy balance. Once this temperature is determined, the second elimination pass determines the other unknown nodal temperatures at each of the in-depth nodes.

General Surface Energy Balance

The events at the heated surface are determined by convective heating and by the surface thermochemical interactions with the boundary-layer gases. Figure 2 illustrates the energy fluxes of interest at the surface. The surface energy balance equation employed is of the convective transfer coefficient type. This energy balance equation takes the following form:

$$\rho_e u_e C_H\left(h_r - h_{e_w}\right) + \rho_e u_e C_M\left[\sum_i \left(Z_{i_e}^* - Z_{i_w}^*\right)h_i^{T_w} - B'h_w\right] + \dot{m}_c h_c + \dot{m}_g h_g + \alpha_w q_{\text{rad}} - F\sigma\varepsilon_w T_w^4 - q_{\text{cond}} = 0$$

The energy fluxes described in the preceding equation represent the sensible convective heat flux, the chemical energy flux, the fluxes entering the control volume from within the solid material, the net radiative heat flux, and the energy conducted into the body. From the first pass of the tridiagonal reduction of the in-depth solution, the conduction term can be expressed as

$$q_{\text{cond}} = AT_w + B$$

This expression may be substituted into the surface energy balance and yields a nonlinear equation in T_w that is solved iteratively by a Newton–Raphson method.

Results

Four test cases are presented that demonstrate the capabilities of the code and compare the predictions with other procedures and/or experimental data. The first two test cases demonstrate the prediction of the surface pressures on blunt and sharp-nosed vehicles. The third case compares the predicted shape of an ablating nosetip with arc heater data, whereas the fourth case compares predicted in-depth temperatures with flight data. The fifth case is a demonstration of the code's abilities to model complete finned body geometries under test or flight conditions.

Apollo Pressure Predictions

Surface pressure distributions on a subscale model of the Apollo capsule are presented in Refs. 10 and 11. The Apollo capsule is a very blunt configuration, and these comparisons demonstrate the code's ability to predict the surface pressure on blunt vehicles. These two tests were also done in two different gases. Bertin's[11] tests were done in air at Mach 9, whereas the Marvin et al.[12] tests were conducted in helium at Mach 20. Figure 5 compares the MASCC pressure prediction with Bertin's data at $\alpha = 0$ deg. The distribution

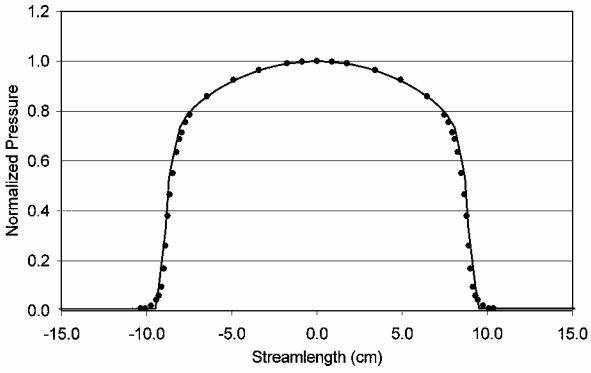

Fig. 5 Pressure comparisons with Apollo data for air at Mach 9.

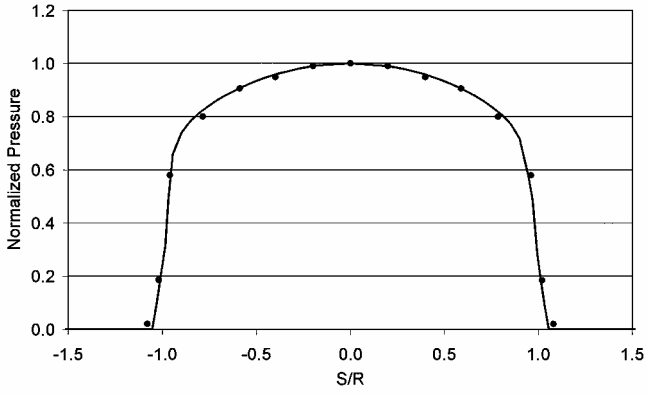

Fig. 6 Pressure comparison with Apollo data in helium at Mach 20.

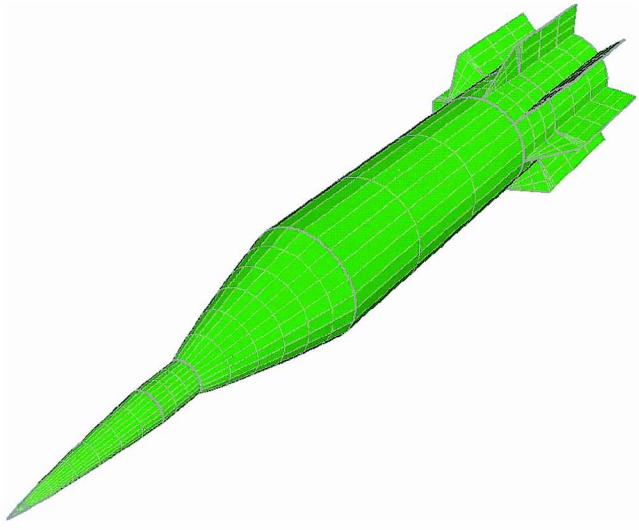

Fig. 7 Tactical missile configuration.

is in excellent agreement with the measurements. Figure 6 shows the predicted distribution in helium. This required a new set of gas properties in MASCC and exercised the new Mollier option in the code. This option allows the user to input a Mollier table for different gases instead of using the air tables that were built into the original code. Again, the agreement with the experimental data is excellent.

Tactical Missile Pressure Predictions

The second test case is for a sharp-nosed, multiconic configuration and compares the predicted surface pressures with CFD results. The vehicle in this study is a prototype tactical missile airframe and the surface patches are shown in Fig. 7. The vehicle consists of an ogive radome with a cylindrical centerbody. The launch configuration has a booster motor and shroud around the center body as shown in Fig. 7. Comparisons have been made with solutions using the GASP code. The pressure predictions along the windward and leeward

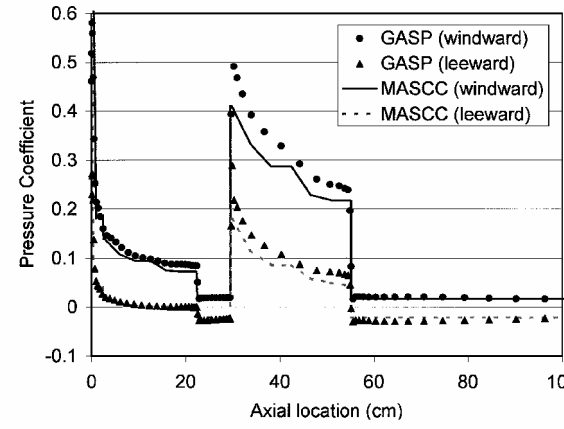

Fig. 8 Pressure comparison with CFD predictions for the tactical missile configuration.

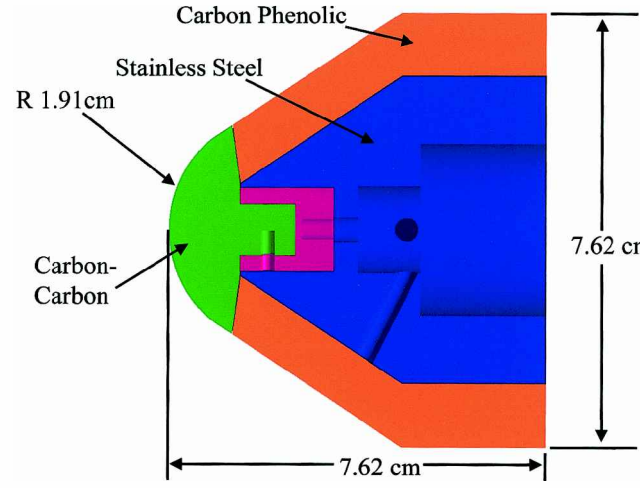

Fig. 9 Schematic of arc heater test article.

streamlines are shown in Fig. 8. The pressures on the ogive and cylindrical portions of the missile are in good agreement with the GASP solution. On the shroud, MASCC underpredicts the pressure. This is probably due to the secondary shock that is formed by the compression on the shroud.

Arc Heater Material Test

Arc heater tests were recently performed at the U.S. Air Force's Arnold Engineering Development Center (AEDC) to evaluate the carbon–carbon and carbon–phenolic materials used for reentry vehicle applications. A subscale test article was developed and tested in the HEAT H1 facility at the AEDC in Tullahoma, Tennessee.[13] During these tests, cameras were used to gather photographic data on the shape and recession of the test article. These data are used for comparison with predictions by the MASCC/CMA code.

The test article consisted of a carbon–carbon nosetip with a 30-deg carbon phenolic heatshield, as shown in Fig. 9. The carbon–carbon was modeled as a subliming ablator, whereas the carbon–phenolic used decomposition kinetics to model the pyrolysis of the phenolic resin. Both surface materials had a stainless steel, nondecomposing backup material at each location.

The predicted shape at the end of the 10-s test is shown in Fig. 10. The one-dimensional conduction model used in MASCC is compared with the results from the experiment and with a calculation using the two-dimensional conduction model in the ASCC. The ASCC calculation did not use the decomposition kinetics in the carbon–phenolic material, and the surface thermochemistry tables had to be modified to account for the energy from the in-depth decomposition. The agreement of both solutions with the experimental data is very good. The recession at the stagnation point and the shaping of the test article is well predicted by both codes.

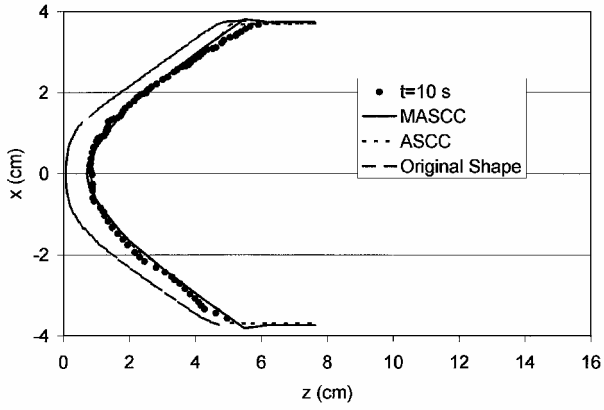

Fig. 10 Measured and predicted shapes.

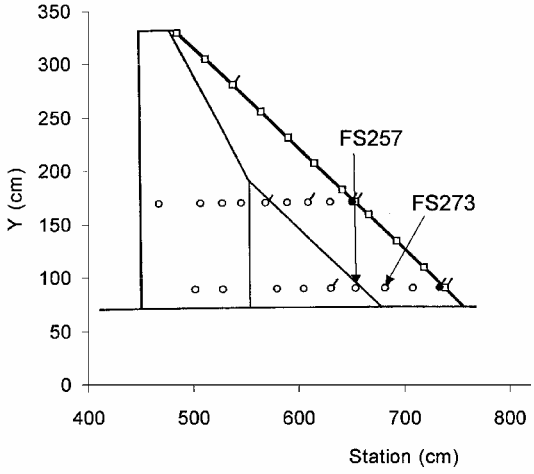

Fig. 11 Sensor locations on the wing lower surface.

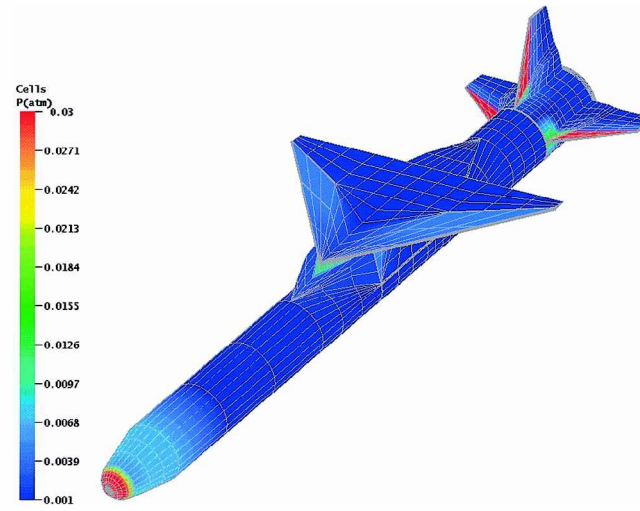

Fig. 12 Surface pressures at 82 s into the flight.

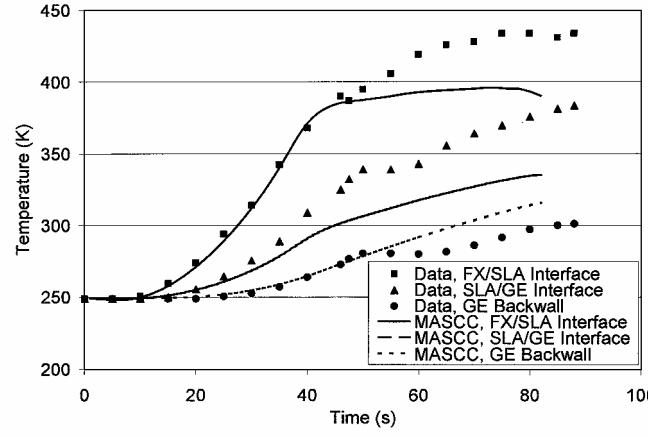

Fig. 13 Temperature comparisons at station FS273 on the lower wing.

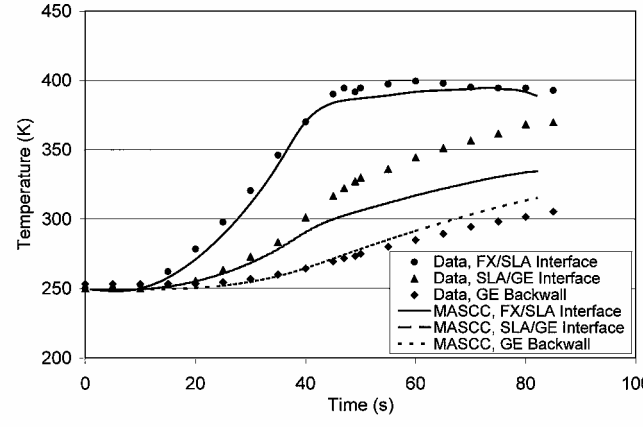

Fig. 14 Temperature comparisons at station FS257 on the lower wing.

Pegasus® Flight Case

The fourth test case uses data from some of the first Pegasus flights. Pegasus is a 15-m air-launched rocket that is dropped at 13 km from a carrier airplane. The rocket uses a delta wing with at span of 6.75 m to provide additional lift in the lower atmosphere and has three fins on its first stage for aerodynamic control. After being released from the carrier aircraft, the rocket pitches up to 20-deg angle of attack for the first 20 s of its flight. Over the next 30 s, the rockets pitches down to 0-deg angle as it flies through 27 km. During the first-stage burn, the rocket continues to accelerate until it reaches $M = 8$ at 62 km. The data used for these comparisons are on the lower surface of the wing.

The thermal protection systems (TPS) used on the early Pegasus vehicles consisted of a two-layer design. The first layer was a low-temperature ablator, and the second layer was a foam or cork insulator. On the wing, the first layer was 0.038 cm of a melting material known as FireX. This material melts at 394 K and the melt flow carries heat away from the surface. The insulating layer on the wing was 0.101 cm of a silica microballoon-filled silicone foam (SLA) developed as a heatshield for space probes. The skin of the wing is composed of 0.101 cm of graphite epoxy. The first Pegasus flights were instrumented with thermocouples between the layers on the TPS and on the back of the graphite-epoxy (GE) skin. Figure 11 presents the locations on the TPS sensors on the lower surface of the wing.

Previous analytical models of the Pegasus airframe considered the fuselage, wing, and fins as separate entities. The previous versions of the code were not able to model configurations as complex as the complete Pegasus airframe. The new version of MASCC has significant simplifications in the input and enhancements in the streamline tracing logic that allow the modeling of the entire body. The surface patch configuration, shown in Fig. 12, used 168 patches and 2016 in-depth thermal solutions. The analysis used the trajectory and heating data from the first Pegasus flight.[14] There were 64 complete flowfield solutions obtained to model the variation of the freestream conditions during the 82 s of the first-stage ascent. The calculation required 6.9 min on a 300-MHz Pentium processor. Pressure contours at the end of the first-stage burn are shown in Fig. 12

Figures 13 and 14 compare the in-depth thermal response at two locations on the lower wing. These locations are FS273 and FS257, both on the inboard row of sensors. FS273 is located at the end of the forward ramp and FS257 is located on the flat portion of the wing just behind the junction with the forward ramp.

The temperature measurements were taken at the interfaces between the various layers of the TPS. The temperatures shown in Fig. 13 are at the interfaces between the FireX and the SLA, the

SLA and the GE skin, and at the back of the wing's skin. Also shown are the CMA predictions from the coupled MASCC/CMA code. The FireX/SLA temperatures maintain very good agreement until 40 s into the flight. At that time, there is an anomaly in the thermocouple response, and the temperature exceeds the melting temperature of the FireX. This anomaly is also seen in the temperatures at the other two locations. This may be caused by the FireX melting away completely, or perhaps by a mechanical failure at one of the interfaces.

The solution underpredicts the temperature at the SLA/GE interface but is in excellent agreement with the backwall temperature up to the point of the anomaly. The underprediction of the SLA/GE interface could be caused by a variation in the thickness of the SLA layer or by inconsistencies in the property models of the SLA. However, because the backwall temperature is well predicted, there may be some bias in the thermocouple data at the SLA/GE interface. Noffz et al.[14] noted a larger than expected lag in the response of the backwall measurements. The present analysis indicates that the bias may actually be at the SLA/GE interface.

Figure 14 compares the in-depth temperatures at FS257. At this station, there was no anomaly in the thermal response at the first interface, and the prediction is in good agreement with the data. At the SLA/GE interface, the prediction is significantly lower than the measurement. Some of the bias noted at FS273 may be present, but at this station the backwall temperature was overpredicted. The lag between the surface and the backwall temperatures for the GE is much smaller than indicated by the data and is more consistent with the thermal properties of the GE. The differences at this station could be due to a bias in the thermal data at the SLA/GE interface and some inconsistencies in the material models or the application of the TPS.

Demonstration Case

Figure 15 provides a three-dimensional view of an airframe prototype design. As can be seen, canards are located on the ogive and fins are utilized with electronics pods at the aft end. The airframe design is composed of a GE motor case, high-temperature materials for fins and canards, and a lightweight metallic ogive. External heatshields are utilized throughout the airframe to allow use of low-temperature, low-weight structural materials.

The demonstration case presented here is for a future lethality sled test type environment to be conducted at the Holloman High Speed Test Track.[15,16] Typically, the payload is a simulant of the system of interest with a defined target located at the end of the track (impact site). The simulant is propelled down the track in multiple stages, achieving velocities in excess of 2000 m/s at the point of impact. The first stage generally starts in air and enters helium at approximately 1000 m/s. The remainder of the trajectory is helium in an effort to reduce heating on the sled and slipper hardware. The uniqueness of MASCC in analyzing these environmental effects on the airframe is the coupling of fin and airframe geometries along with multiple medium effects.

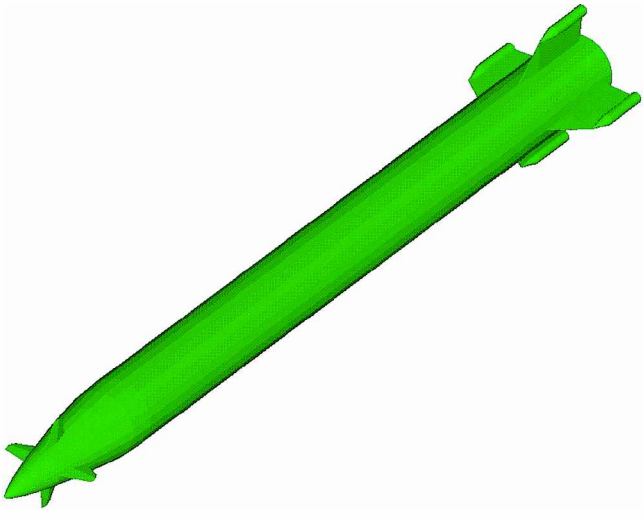

Fig. 15 Surface patch configuration for sample missile configuration.

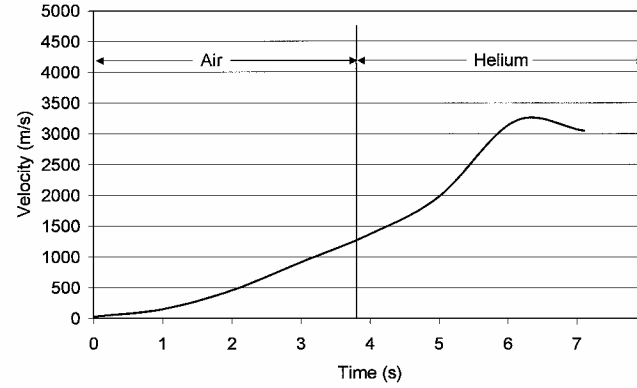

Fig. 16 Typical lethality sled trajectory.

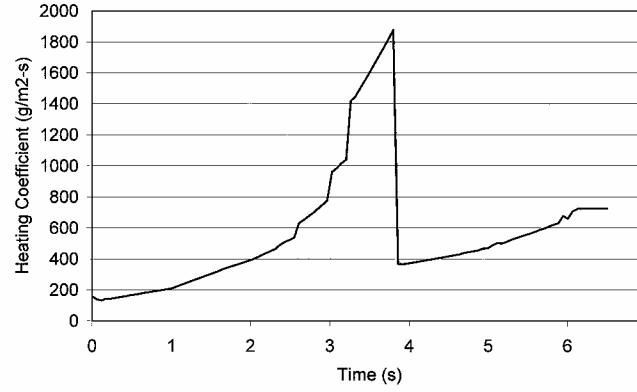

Fig. 17 Sled test predicted heating on the fore cone.

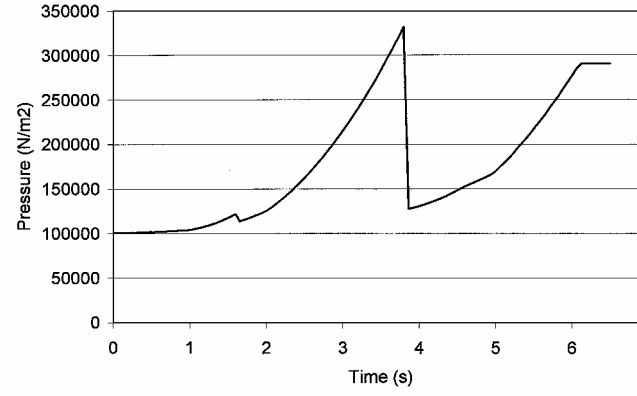

Fig. 18 Sled test predicted pressures on the fore cone.

An example trajectory of a lethality sled test is shown in Fig. 16. As can be seen, a peak of 3000 m/s is obtained at the point of impact. The vehicle enters the helium bag at approximately 3.7 s and remains in helium until impact. Figure 17 provides the heat transfer coefficient history for the fore cone of the ogive. As can be seen, a significant reduction in coefficient occurs when the vehicle enters the helium environment. Figure 18 provides the pressure history prediction for the fore cone and shows a similar reduction when the vehicle enters the helium.

Figures 19 and 20 are contour plots of the surface temperature response before the vehicle enters the helium environment. Temperature gradients are shown from the hottest leading edges to the coolest sections on the cylindrical body. Figure 19 presents the surface temperatures on the ogive and canards. This plot shows the details on the canards and the hotter portions of the ogive. Figure 20 presents the surface temperatures on the aft fins. Here, the higher heating on the leading edges of the fins and the electronics pods is clearly visible.

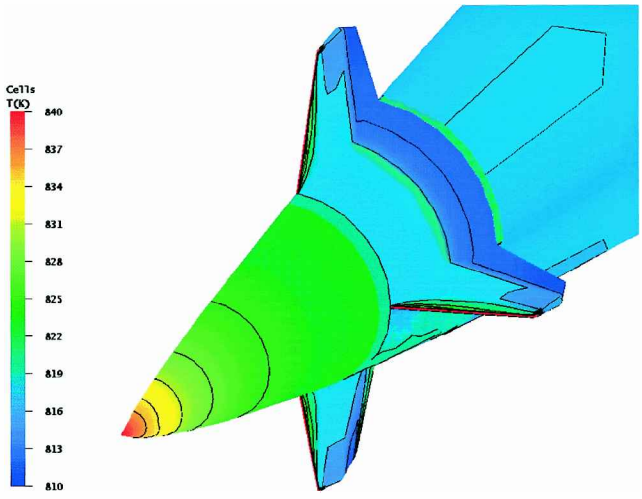

Fig. 19 Predicted surface temperature on the nose of the sample missile configuration.

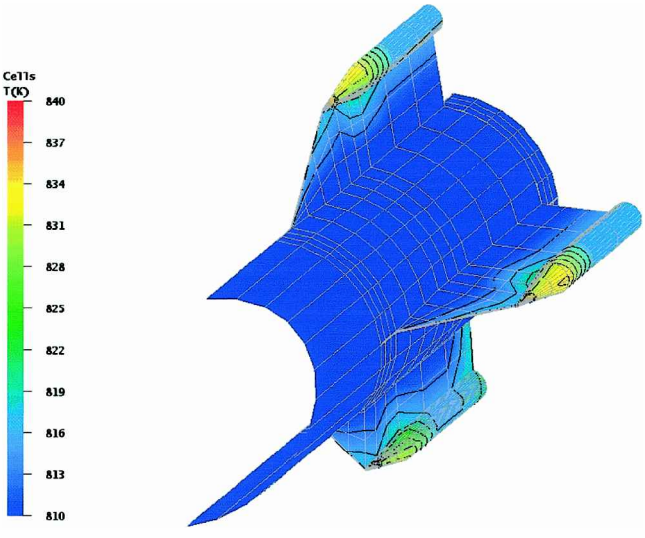

Fig. 20 Predicted surface temperatures on the fins of the sample missile configuration.

The plots presented here are limited to the air environment just before the helium is entered. Enhancements and refinements are currently being incorporated into the software to allow for surface energy balance and in-depth conduction in multiple medium environments.

Conclusions

A one-dimensional thermal solution technique has been incorporated into MASCC. Comparisons with data from arc heater tests have shown that the new code accurately predicts surface recession and temperature. Flight-data comparisons have shown that the code is able to predict in-depth temperatures on complete winged body configurations. A calculation was performed using a multiple environment (air/helium) to demonstrate the ability to model changes in the freestream gas. This capability is useful for predictions of ballistic ranges or sled tests where different gases are necessary to obtain data of interest.

References

[1]Murray, A. L., "User's Manual for the Maneuvering Aerotherm Shape Change Code (MASCC99)," Aerotherm Corp., FR 6002-99-001, Huntsville, AL, Jan. 1999.

[2]"User's Manual: Aerotherm Charring Material Thermal Response and Ablation Program," Acurex Corp., Rept. UM-87-11/ATD, Mountain View, CA, Aug. 1987.

[3]Coons, S. A., and Herzog, B., "Surfaces for Computer-Aided Aircraft Design," AIAA Paper 67-895, 1967.

[4]Dahm, T., Cooper, L., Rafinejad, D., Youngblood, S., and Kelly, J., "Inviscid Flow and Heat Transfer Modeling for Reentry Vehicle Nosetips," Space and Missile Systems Organization, SAMSO-TR-77-11, Los Angeles, Nov. 1976.

[5]Andrews, J. S., "Steady State Airload Distribution on Hammerhead Shaped Payload of a Multistage Vehicle at Transonic Speeds," The Boeing Co., Rept. D2-22947-1, Seattle, WA, Jan. 1964.

[6]Isaacson, L. K., and Jones, J. W., "Prediction Techniques for Pressures and Heat-Transfer Distributions Over Bodies of Revolution in High-Subsonic to Low-Supersonic Flight," U.S. Naval Weapons Center, Rept. NWC TP 4570, China Lake, CA, Nov. 1968.

[7]Timmer, H. G., "Ablation Aerodynamics for Slender Reentry Bodies," U.S. Air Force Flight Dynamics Lab., Rept. AFFDL-TR-70-27, Dayton, OH, March 1970.

[8]Kutateladze, S. S., and Leont'ev, A. I., *Turbulent Boundary Layers in Compressible Gases*, Academic Press, New York, 1964, pp. 16–20.

[9]Kutateladze, S. S., "On the Turbulent Boundary Layer with Vanishing Viscosity," *Heat and Mass Transfer in Boundary Layers, Volume I, Proceedings of the International Summer School, Heat and Mass Transfer in Turbulent Boundary Layers, Herceg Novi, September 1969*, edited by N. Afgan, Z. Zaric, and P. Anastasijevic, Pergamon, New York, 1972, pp. 9–50.

[10]Murray, A. L., and Wolf, C. J., "Three-Dimensional Boundary Layers on Reentry Vehicles—Engineering Documentation and Computer Code User's Manual," Acurex Corp., Rept. FR 81-27/ATD, Mountain View, CA, Dec. 1981.

[11]Bertin, J. J., "Wind-Tunnel Heating Rates for the Apollo Spacecraft," NASA TM X-1033, Jan. 1965.

[12]Marvin, J., Tendeland, T., and Kussoy, M., "Apollo Forebody Pressure and Heat-Transfer Distributions in Helium at $M_\infty = 20$," NASA TM X-854, Nov. 1963.

[13]"Performance Measurement of the CHOP SM-14 Thermal Protection System," Aerotherm Corp., Rept. FR 756A150-2000-27, Huntsville, AL, April 2000.

[14]Noffz, G., Curry, R. E., Haering, E., and Kolodziej, P., "Aerothermal Measurements from the Pegasus® Air Launched Space Booster; Flight 1," NASA TM 4330, Oct. 1991.

[15]Russell, G. W., "PATRIOT PAC-3 Lethality Sled Test Long Body Fin Section Thermal Analysis," U.S. Army Missile Command, TR RD-PS-98-3, Redstone Arsenal, AL, Feb. 1998.

[16]Thomas, D. T., and Russell, G. W., "Thermal Protection Requirements for the Super Road Runner Motor Development Program," U.S. Army Aviation and Missile Command, Letter Rept. RD-PS-99-12, Redstone Arsenal, AL, Feb. 1999.

T. C. Lin
Associate Editor

Color reproductions courtesy of the U.S. Army Aviation and Missile Command.